nature portfolio

https://doi.org/10.1038/s41567-020-01161-4

Supplementary information

Quantum sensing of a coherent single spin excitation in a nuclear ensemble

In the format provided by the authors and unedited

Quantum sensing of a coherent single spin excitation in a nuclear ensemble: Supplementary information

D. M. Jackson [1*], D. A. Gangloff [1*†], J. H. Bodey [1], L. Zaporski [1], C. Bachorz [1], E. Clarke [2], M. Hugues [3], C. Le Gall [1], and M. Atatüre[1 †]

[1] *Cavendish Laboratory, University of Cambridge, JJ Thomson Avenue, Cambridge, CB3 0HE, UK*
[2] *EPSRC National Epitaxy Facility, University of Sheffield, Broad Lane, Sheffield, S3 7HQ, UK*
[3] *Université Côte d'Azur, CNRS, CRHEA, rue Bernard Gregory, 06560 Valbonne, France*

[*] *These authors contributed equally to this work.*
[†] *e-mail: dag50@cam.ac.uk; ma424@cam.ac.uk.*

CONTENTS

I. RAMAN-BEAM CONSTRUCTION

The Raman laser source is a TOPTICA TA Pro. Raman beams are generated by modulating a fiber-based EOSPACE electro-optic amplitude modulator (EOM) with a microwave tone constructed as follows. A Rohde & Schwartz 22-GHz microwave frequency source generates a fixed amplitude tone at 11 GHz, which is frequency mixed (Mini Circuits mixer ZX05-24MH-S+) with the output of a Tektronix arbitrary waveform generator (AWG70001A, 25 GSamples/s) operated at approximately 3 GHz. The mixer output is high-pass filtered to remove undesired frequency components and retain only a tone at apporximately 14 GHz, which is amplified to a peak power of 25 dBm. The Raman beams, with a combined optical power of around 1 mW at the device, are passed through a quarter-wave plate and arrive at the quantum dot with near circular polarization. The first-order EOM sidebands are two coherent laser fields whose energy difference can be made resonant with the electron spin resonance (ESR), as per this work 28 GHz (corresponding to an applied magnetic field $B_z = 4.5\,\mathrm{T}$), leading to a two-photon detuning $\delta \approx 0$. The Raman beams have a single-photon detuning of $\Delta \gtrsim 800\,\mathrm{GHz}$, which is much larger than trion linewidth of $\Gamma_0 = 150\,\mathrm{MHz}$, as is typical for this sample. Spontaneous scattering from the trion manifold is approximately $\Gamma_0\Omega/4\Delta \approx 0.5\,\mathrm{kHz}$, given a *qubit-drive* (two-photon) Rabi frequency of $\Omega = 10\,\mathrm{MHz}$. This scattering rate is much smaller than the relevant relaxation and dephasing rates in the system and as such can be neglected during magnon creation.

II. PULSE SEQUENCES

A single repeating unit of the full experimental pulse sequence is depicted schematically in Fig. S1. It is split into two very similar sequences, which differ only in the electron spin population that is interrogated. Both are preceded by $T_{\mathrm{prep}} = 11\,\mu\mathrm{s}$ of nuclear spin preparation, unless otherwise stated, equating to a preparation ratio of $T_{\mathrm{prep}}/T_{\mathrm{exp}} \sim 3$. This preparation ensures we always perform our sensing sequences with a cooled nuclear spin

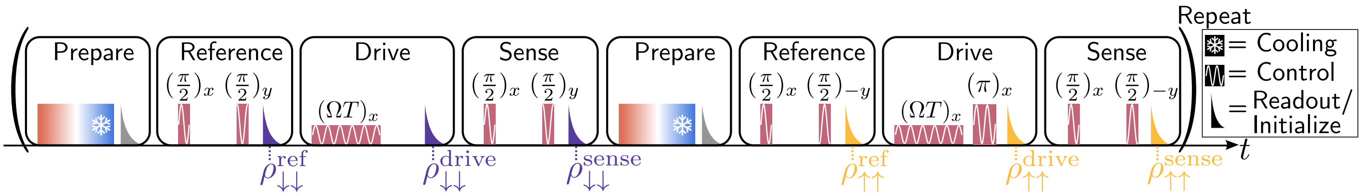

Fig.S1. **Experimental pulse sequence.** Full experimental pulse sequence for magnon sensing. Timings are not to scale; preparation (red-blue pulses) typically has a 70% duty cycle. The two halves of the sequence differ only in which electron spin population is probed (purple versus yellow readout pulses). Spin rotations on the electron (pink pulses) are labelled with the rotation angle and axis of rotation on the Bloch sphere; the inlaid white curves depict the qubit drive field, and show how steps in its phase can control the axis of rotation.

bath. Cooling is performed by driving the electron spin with a Rabi frequency, Ω_{cool}, of 13 MHz whilst exciting resonantly the optical transition between electron spin-↓ and the lowest-energy trion excited state, with a saturation parameter of 0.5. This resonant excitation optically pumps the electron, which engineers an effective linewidth for the spin-↓ state of $\Gamma_{\text{p}} = 35\,\text{MHz}$[1].

To interrogate the electronic populations we again optically pump the electron from spin-↓ to spin-↑ via the excited trion state. We do so for 150 ns, which is much longer than the optical pumping time (approximately 2 ns), in order to reach high-fidelity initialization. The resulting brightness, integrated over the first 50 ns of this readout pulse, is directly proportional to spin-↓ population, $\rho_{\downarrow\downarrow}$. In the second half of the experimental sequence we precede this readout with a spin inversion of the electron (Fig. S1), yielding a brightness which is instead proportional to spin-↑ population, $\rho_{\uparrow\uparrow}$; in this way we can extract both populations and thus electron spin polarization $S = \rho_{\downarrow\downarrow} - \rho_{\uparrow\uparrow}$. Taking the normalized difference of our readouts to obtain spin polarization allows us to cancel any noise that would arise from a drift in outcoupling efficiency.

III. CALIBRATIONS

Before any experiment we calibrate the Ramsey control sequence used for magnon sensing. Specifically we aim to configure the Ramsey interferometer in the ideal *side-of-fringe* configuration, which is maximally sensitive to small magnon-induced ESR frequency shifts. Firstly, we calibrate the qubit-drive pulse duration required in order to perform a $\frac{\pi}{2}$-rotation of the electron spin, which is simply a quarter of a Rabi period. To this end we drive Rabi oscillations of the qubit for many periods (Fig. S2a) to extract the Rabi frequency, $\Omega = 280\,\text{MHz}$, and thus the gate time, $1/4\Omega = 0.89\,\text{ns}$. Secondly, we calibrate the drive frequency used for the $\frac{\pi}{2}$-rotations. In the ideal case, we simply set this to the bare ESR frequency, meaning all rotations occur in a frame rotating with the qubit. In reality, there are two systematic pulse errors that we calibrate and correct using appropriate drive detunings, as detailed below. In this way we ensure that the rotating frame of the drive matches the qubit at all times.

A. Pulse compensation

The high optical power used during a $\frac{\pi}{2}$-pulse leads to a differential optical Stark shift on the two spin eigenstates. If left unchecked, this effective detuning of the qubit drive leads to rotations which are not about the desired axes. We compensate this effect by changing the drive frequency used during the pulse by δ_{pulse} to match the shifted qubit frequency. To find the correct δ_{pulse} we use a *side-of-fringe* Ramsey sequence with zero Ramsey delay ($\tau = 0$), i.e. a $(\frac{\pi}{2})_x$ rotation followed immediately by a $(\frac{\pi}{2})_y$ rotation (Fig. S2b inset). At the zero-crossing of electron polarization, S, versus δ_{pulse} (orange circles), we have applied the correct detuning, $\delta_{\text{pulse}} \approx -20\,\text{MHz}$, to configure the Ramsey interferometer on the *side-of-fringe*.

B. Free-precession compensation

The second systematic pulse error is a detuning originating from the nuclear-preparation step of the experimental sequence (Fig. S1). We engineer feedback on the nuclear polarization in order to lock the ESR frequency to that of our qubit drive. With the drive frequency set equal to the bare ESR, this defines a lockpoint around zero nuclear polarization, $\langle I_z \rangle \approx 0$[1]. Crucially, part of this feedback requires resonant pumping of the optical transition to the trion manifold, which optically Stark shifts the lockpoint away from the drive frequency by a few megahertz. Such a shift between the locked ESR frequency and the drive is precisely what we detect during the free precession of a Ramsey sequence. Indeed it would be added to any magnon-induced ESR shift we hope to measure, obfuscating single-magnon detection. To this end, we cancel the optically induced ESR shift with an opposite detuning on the qubit drive, δ_{free}, during free precession. Since the drive is off during this time, a detuning is instead applied as a phase, $2\pi\delta_{\text{free}}\tau$, to the second Ramsey pulse. To find the correct δ_{free} we use a *side-of-fringe* Ramsey sequence with a finite delay (Fig.

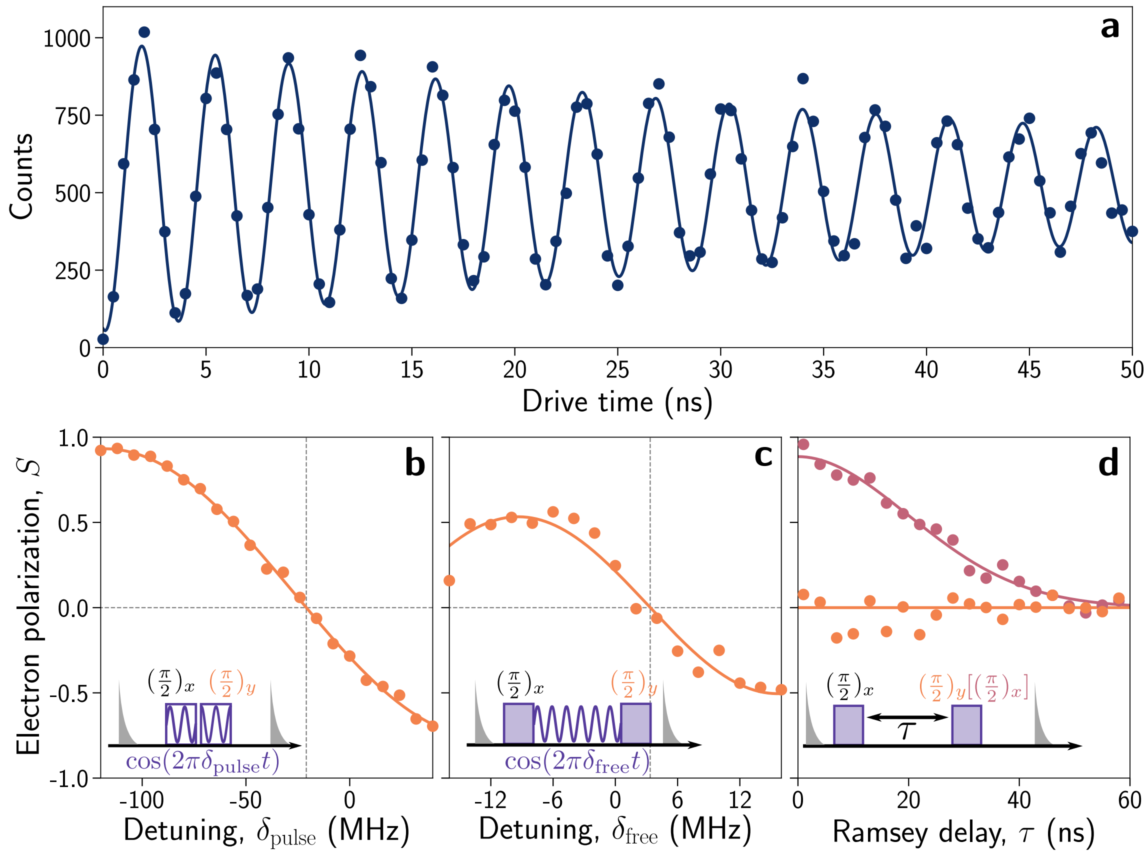

Fig.S2. **Ramsey interferometry calibrations. a,** Rabi oscillations of the electron spin (blue circles) fitted with a mono-exponentially decaying sinusoid[2] (solid curve). These counts are obtained after 4s of a sequence with a readout duty cycle as in Fig. S1. From this we extract a Rabi frequency of $\Omega = 280$ MHz and thus calibrate the pulse duration required for $\frac{\pi}{2}$-rotation, i.e. $1/4\Omega = 0.89$ ns. **b,** Compensating a systematic pulse error present during each $\frac{\pi}{2}$-rotation in our Ramsey sequence. Electron polarization measured after a *side-of-fringe* Ramsey sequence at zero delay (inset) is plotted versus the correction detuning, δ_{pulse}, (orange circles). A sinusoidal fit (solid curve) yields a zero-crossing of $\delta_{\mathrm{pulse}} \approx -20$ MHz. **c,** Compensating a systematic detuning present during free precession. Electron polarization measured after a *side-of-fringe* Ramsey sequence at finite delay, $\tau \approx 20$ ns, (inset) is plotted versus the correction detuning, δ_{free}, (orange circles). A sinusoidal fit (solid curve) yields a zero-crossing of $\delta_{\mathrm{free}} \approx -3.5$ MHz. **d,** Ramsey interferometry signals after careful calibration for both *top-of-fringe* (pink circles) and *side-of-fringe* (orange circles) configurations. The former is fitted to a Gaussian free-induction decay (pink curve), from which we obtain the characteristic decay time $T_2^* \approx 30$ ns. In the latter, electron spin polarization is pinned to 0 (orange curve), i.e. the side of a Ramsey fringe.

S2c inset), again looking for the zero crossing of electron polarization versus δ_{free}. At this point the rotating frame defined by the drive frequency is matched precisely to the qubit. This means that as we scan τ in Fig. S2d (orange circles) there is no phase accumulation of the qubit, and electron polarization is pinned to the *side-of-fringe*.

IV. RAMSEY MEASUREMENTS

A. Optimal Ramsey sequence

Having calibrated our Ramsey interferometer to the *side-of-fringe* configuration, we expect the signal in electron polarization to obey the following equation:

$$S^{\mathrm{sense}} = \rho_{\downarrow\downarrow}^{\mathrm{sense}} - \rho_{\uparrow\uparrow}^{\mathrm{sense}} = e^{-(\frac{\tau}{T_2^*})^2} \sin(2\pi\tau\Delta\omega_{\mathrm{sense}}). \quad (1)$$

Here we map a small phase angle, $2\pi\tau\Delta\omega_{\mathrm{sense}}$, to a change in electron polarization linearly, compared to a *top-of-fringe* configuration, which goes as $\cos(2\pi\tau\Delta\omega_{\mathrm{sense}})$, where there is a less sensitive quadratic mapping. Both situations are depicted in Fig. S2d for $\Delta\omega_{\mathrm{sense}} = 0$. In the latter configuration we can extract the characteristic decay time $T_2^* \approx 30$ ns, which sets the maximum Ramsey delay we can use for sensing before the qubit loses its coherence. During this time the phase accumulation we expect due to a 200-kHz ESR shift is only about 0.01π. For small angles such as this, a linear mapping to electron polarization is clearly advanta-

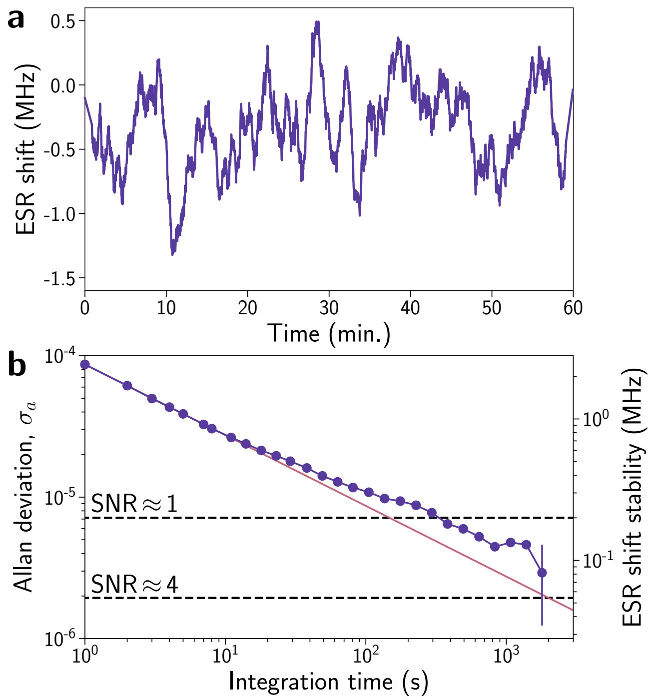

Fig.S3. **Allan deviation of ESR frequency. a,** Time trace of repeated measurements of the ESR shift, $\Delta\omega_{\mathrm{ref}}$, (purple curve). **b,** Purple curve is the overlapping Allan deviation, σ_{a}, calculated from the above time-series, as a function of integration time; i.e. the time over which we average the measured ESR shift. We multiply the dimensionless σ_{a} by the qubit frequency, ω_{e}, to obtain the absolute ESR-frequency stability on the right axis. The single-magnon ESR shift is approximately 200 kHz, which defines the signal-to-noise ratio (SNR) thresholds depicted. The extrapolated short-time behaviour (pink curve) scales inversely with the square root of the integration time.

geous. To a good approximation the expected signal is then $S^{\mathrm{sense}} \approx e^{-(\tau/T_2^*)^2} 2\pi\tau\Delta\omega_{\mathrm{sense}}$, which has a maximum at $\tau = T_2^*/\sqrt{2}$. As such we conclude that a Ramsey interferometer configured on the *side-of-fringe* and fixed at this delay is the most sensitive sequence for detecting sub-200 kHz ESR shifts[3].

B. Sensor performance: Allan deviation

We characterize sensor performance by using our precision Ramsey sequence to make repeated measurements of the *reference* ESR shift, $\Delta\omega_{\mathrm{ref}}$, at a sampling rate of 1 Hz. The time-trace of these measurements over the course of one hour is presented in Fig. S3a, where we have smoothed the data with a 100 s moving average. Since there is no magnon injection we expect to measure no shift from the bare electron spin splitting, and so an average $\Delta\omega_{\mathrm{ref}} = 0$. There is, however, a small $\approx$ 500-kHz error in the δ_{free} calibration, which has shifted the mean; this has no consequence for the following discussion as we only seek to quantify the variations in $\Delta\omega_{\mathrm{ref}}$. From the time trace in Fig. S3a we can see qualitatively that there are slow drifts in the ESR shift on top of higher frequency noise. To quantify this we calculate the Allan deviation[4] from our series of $m = 3600$ samples $\{\Delta\omega_i^{\mathrm{ref}}\}$, which we first divide by the qubit frequency, ω_{e}, to obtain dimensionless, fractional frequencies $\{f_i^{\mathrm{ref}}\}$. For an integration time of n seconds, the overlapping Allan variance[5] is then given by

$$\sigma_{\mathrm{a}}^2(n) = \frac{1}{2n^2(m-2n+1)} \sum_{j=0}^{m-2n} \left(\sum_{i=j}^{j+n-1} f_{i+n}^{\mathrm{ref}} - f_i^{\mathrm{ref}} \right)^2 . \tag{2}$$

The square-root of this quantity—plotted in S3b as a function of the averaging time (purple circles)—is a metric of the fluctuations in the qubit frequency. We are characterising fluctuations in the ESR frequency with precisely the method we use to detect the single magnon ESR shift. As such this metric captures all the noise sources we can expect to limit the precision of an ESR shift measurement. Due to technical limitations on our total experimental time, the maximum achievable integration time per data point is 2000 s. In this regime, fluctuations in ESR shift are twice what would be expected from the quantum-limited noise of our photonic readout, which is given by the extrapolation of the short averaging-time behaviour. These low-frequency additional noise sources could arise from slow drifts in either the resonant laser power, altering the systematic detuning δ_{free} calibrated for in section III B, or the Raman laser polarization, affecting the systematic detuning δ_{pulse} calibrated for in section III A. Variations in both of these systematic detunings would manifest as noise on the measured ESR shift. Regardless of the source, we outline in the main text how these slow drifts can be bypassed with a differential measurement.

V. MODELLING MAGNON DYNAMICS AS SIMPLE HARMONIC MOTION

In order to efficiently extract the *activated exchange* frequency at each drive frequency Ω from our complete set of data (see also section VI of this supplementary) – the summary of which is presented in Fig. 4d of the main text – we have modelled the injection of a magnon into N nuclear spins as the drive of a two level system with a non-degenerate ground state $|g, \mathcal{T}\rangle$ and an N-fold degenerate excited state $|e, \mathcal{T}\rangle$ (Fig. S4): an exact model for a fully polarized nuclear ensemble. Presently, we neglect an additional state $|g, \mathcal{R}\rangle$ represented in Fig. S4, which later will come to represent the leakage of population from the target manifold $\mathcal{T}$ to an undesired residual manifold $\mathcal{R}$. The single-nucleus Rabi frequency is given by $\Omega' = \alpha\Omega$ where Ω is the qubit-drive Rabi frequency. Working in the rotating frame we then find that

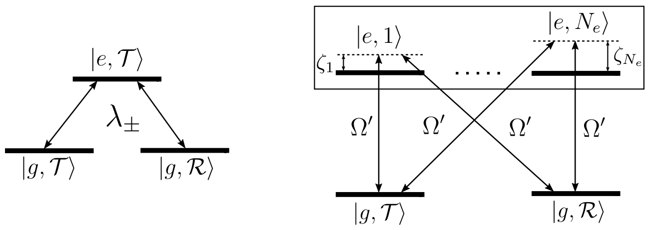

Fig.S4. **Magnon dynamics as a two-level system.** Energy level diagram representing the two-level system $\{|g,\mathcal{T}\rangle\,,|e,\mathcal{T}\rangle\}$ used to model simplified magnon dynamics. The excited state is N-fold degenerate, each with a randomly distributed detuning, ζ_e. Ω' is the single-nucleus Rabi frequency, which couples each degenerate excited state to the ground state. $|g,\mathcal{R}\rangle$ is a single state which models the leakage of population out of the target manifold $\mathcal{T}$.

the probability amplitudes a_g and $\{a_e\}_{1..N}$ for being in the ground and excited states, respectively, are captured by the following equations:

$$\begin{aligned} i\dot{a}_e &= \Omega' a_g e^{i\zeta_e t} \\ i\dot{a}_g &= \Omega' \sum_e a_e e^{-i\zeta_e t} \end{aligned} \tag{3}$$

where we have made the rotating wave approximation. Strain inhomogeneities in a QD couple with the quadrupolar Hamiltonian to produce an inhomogeneous distribution of nuclear resonances[6–8], captured here by a randomly distributed detuning, ζ_e (Fig. S4).

Equations 3 can be decoupled, and expressed through an integro-differential equation after taking $a_g(0) = 1$:

$$\dot{a}_g = -\Omega'^2 \sum_e \int_0^t dt' a_g(t') e^{i\zeta_e(t'-t)} \tag{4}$$

In the asymptotic N-limit, ζ_e is described by a spectral distribution $S(\zeta)$, where $\int d\zeta S(\zeta) = N$, and equation 4 takes the form:

$$\dot{a}_g \xrightarrow{N\to\infty} -\Omega'^2 \int_0^t dt' a_g(t') \int_{-\infty}^{\infty} d\zeta S(\zeta) e^{i\zeta(t'-t)} \tag{5}$$

Assuming a Lorentzian distribution for $S(\zeta)$, with a full width at half maximum of σ_ζ, simplifies equation 5 yielding

$$\dot{a}_g = -N\Omega'^2 \int_0^t dt' a_g(t') \exp\{\sigma_\zeta(t'-t)\} \tag{6}$$

This is a standard example of a Delay Differential Equation, which can be solved exactly. Differentiating equation 6 using the Leibnitz rule, we arrive at a linear second order differential equation:

$$\ddot{a}_g = -N\Omega'^2 a_g - \sigma_\zeta \dot{a}_g \tag{7}$$

which we immediately recognize as that which governs simple harmonic motion. This can be solved easily using the ansatz $a_g \propto e^{\lambda t}$, yielding:

$$\lambda_\pm = -\frac{\sigma_\zeta}{2} \pm \sqrt{\frac{\sigma_\zeta^2}{4} - N\Omega'^2} \tag{8}$$

In this way we have simplified the dynamics of magnon injection to damped simple harmonic motion with a damping rate $\Gamma = \sigma_\zeta/2$ and a collectively enhanced drive strength $\Omega_{\rm exc} = \sqrt{N}\Omega'$.

At this point point we note that the above solution predicts that the probability of being in the ground state at infinite time is zero, while the electron ground-state population in fact equilibrates to 1/2. To account for this we now return to consider the additional ground state $|g,\mathcal{R}\rangle$ in Fig. S4, which captures approximately the leakage of population into the manifold $\mathcal{R}$ consisting of all other consistent ground states in the system. This leakage will be at its maximum in our case since we operate around zero nuclear polarization[9]. With this extension to the above calculation we again recover simple harmonic motion, but crucially we find that the probability to be in this now two-fold degenerate ground state manifold decays to 1/2 as desired. This brings us to Eq. 10 that is used to fit the data presented in the following section.

VI. EXTENDED DATA

A. ESR-shift spectra

In Figs. 3c and 3d of the main text we present the ESR shifts measured after driving the $I_z - 2$ and $I_z - 1$ magnon modes, respectively. Specifically, we plot these shifts, whose magnitude we attribute to dynamic nuclear polarization (DNP) that accumulates from one cycle of the pulse sequence to the next, versus preparation ratio, $r = T_{\rm prep}/T_{\rm exp}$. These shifts have been extracted from the fitted amplitudes of the corresponding spectral features of Fig. S5, where we offset the spectra for clarity. Each spectrum is obtained after 1.8 μs of qubit drive with a Rabi frequency of 8 MHz. For the $I_z - 2$ mode we can extract the amplitude of the spectrally resolved $-2\omega_{\rm n}^{\rm In}$ feature, whereas for the $I_z - 1$ mode we can only fit the unresolved $(-\omega_{\rm n}^{\rm In}, -\omega_{\rm n}^{\rm As})$ feature. Nevertheless, in Fig. S5 we see explicitly the quenching of DNP as we increase the fraction of time spent cooling the nuclear ensemble. As such, for the largest preparation ratio, the spectrum of ESR shift measured prior to exciting a magnon, $\Delta\omega_{\rm ref}$, approaches zero, and that measured after, $\Delta\omega_{\rm sense}$, approaches the single-magnon spectrum. In Figs. 3c and 3d of the main text we capture the r-dependence of the measured ESR shifts with the following phenomenological functional form:

$$\begin{aligned} \Delta\omega_{\rm ref}(r;a,b) &= \frac{a}{1+r/b} \\ \Delta\omega_{\rm sense}(r;a,b,c) &= \Delta\omega_{\rm ref}(r;a,b) + c, \end{aligned} \tag{9}$$

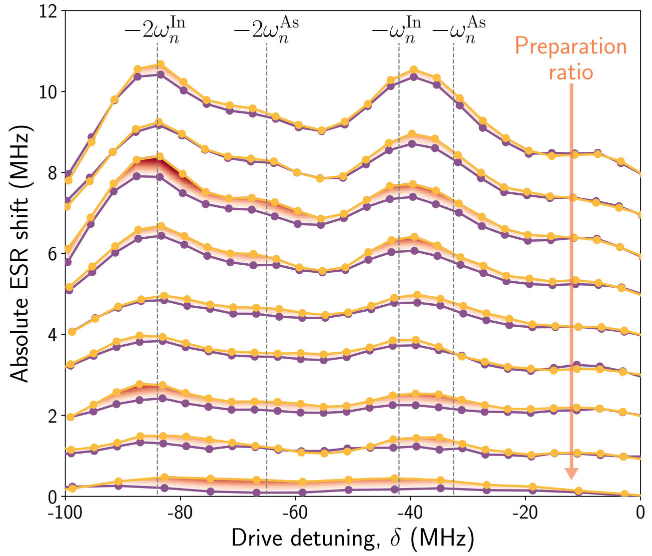

Fig.S5. **ESR shift spectra.** The absolute value of the ESR-shift spectra – for negative drive detunings only – measured during *reference* and *sense* sequences (purple and yellow circles, respectively) for varying preparation ratio. Preparation-ratio ranges from 1.4 (top) to 27.5 (bottom). Solid curves are linear interpolations between data points. Spectra have been offset by 1 MHz for clarity.

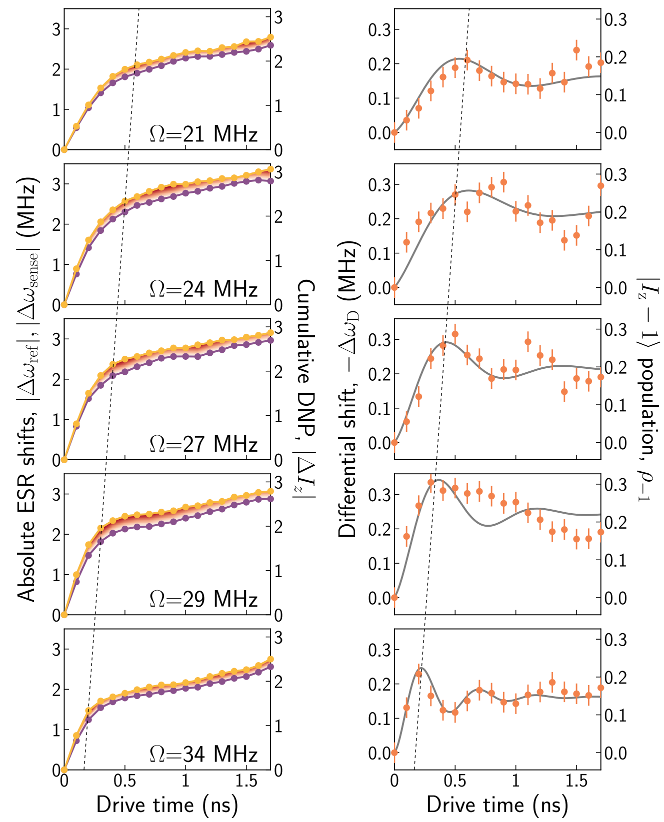

Fig.S6. **Rabi oscillations of $|I_z\rangle \leftrightarrow |I_z-1\rangle$ Indium transition. (left)** Absolute value of the ESR shifts, $|\Delta\omega_{\rm ref}|$ and $|\Delta\omega_{\rm sense}|$, measured during time-resolved driving of the $|I_z\rangle \leftrightarrow |I_z-1\rangle$ transition (purple and yellow circles, respectively). To convert these shifts to the corresponding accumulated DNP (right axis) we divide by $2A_{\rm In}$. **(right)** The difference of these two shifts, $\Delta\omega_{\rm D}$, is the single magnon ESR shift (orange circles). We plot its negative here for clarity, and also convert to population in the $|I_z-1\rangle$ state, $\rho_{-1} = -\Delta\omega_{\rm D}/2A_{\rm In}$, (right axis). We fit the time evolution to that of a damped harmonic oscillator (solid curves). The dotted lines are a guide to the eye, depicting the approximate π-time of the electron-magnon exchange for each drive Rabi frequency, Ω.

where c represents the single-magnon shift. We optimize a, b and c for $\Delta\omega_{\rm ref}$ and $\Delta\omega_{\rm sense}$ simultaneously with a least-squares fitting algorithm. The resulting parameters are $a = 15(8)$ MHz, $b = 0.3(2)$, $c = 210(50)$ kHz for the $I_z - 1$ mode and $a = 9(3)$ MHz, $b = 0.6(3)$, $c = 200(70)$ kHz for the $I_z - 2$ mode.

B. Magnon oscillations

In Figs. S6 and S7 we present supplementary data to Fig. 4 of the main text, which depict the time-resolved ESR shifts under resonant driving of the $I_z - 1$ and $I_z - 2$ modes, respectively. For multiple drive Rabi frequencies we plot both the cumulative and differential shifts, the former being enhanced by the accumulation of DNP because we operate with a preparation ratio of only $T_{\rm prep}/T_{\rm exp} = 3$. For both magnon modes we divide these cumulative ESR shifts by $2A$ to convert to the corresponding DNP, ΔI_z. Similarly, we also convert the differential shift to magnon population in the $|I_z - 1\rangle$ and $|I_z - 2\rangle$ states by dividing by $2A$ and $4A$ respectively. To obtain the drive Rabi-frequency dependence of the coherent dynamics we fit the oscillatory behaviour of $\Delta\omega_{\rm D}$ as a function of drive time T to that of a damped harmonic oscillator, as per section V:

$$\Delta\omega_{\rm D} = \omega_0 \left[1 - \frac{e^{-\Gamma T}}{2}\left(e^{iT\sqrt{\Omega_{\rm exc}^2-\Gamma^2}} + e^{-iT\sqrt{\Omega_{\rm exc}^2-\Gamma^2}}\right)\right]. \tag{10}$$

We leave the fitting algorithm free to explore both the over- and under-damped regimes, but as can be seen from Figs. S6 and S7 it returns under-damped motion as the best fit in all cases. The fitted exchange frequency, $\Omega_{\rm exc}/2\pi$, is what is plotted in Fig. 4d of the main text.

VII. MODELLING THE ELECTRON-NUCLEAR INTERFACE

A. System Hamiltonian

We consider the following system Hamiltonian[1,2,9] representing an electron spin qubit and the collective states of two nuclear species, arsenic (As) and indium (In):

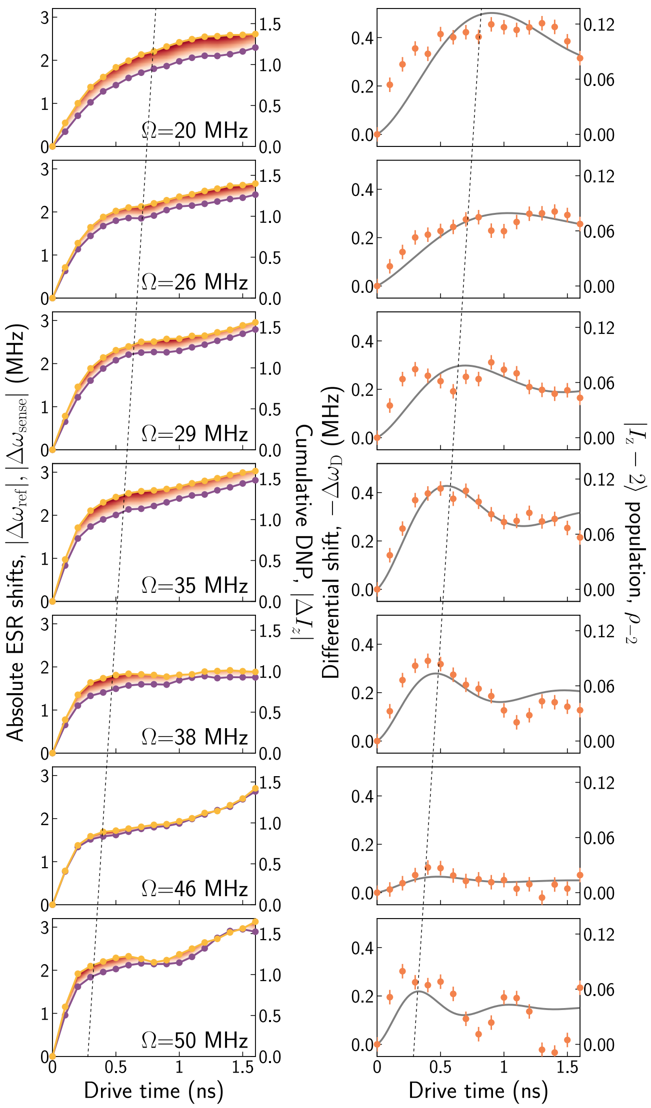

Fig.S7. **Rabi oscillations of $|I_z\rangle \leftrightarrow |I_z-2\rangle$ Arsenic transition.** **(left)** Absolute ESR shifts, $|\Delta\omega_{\mathrm{ref}}|$ and $|\Delta\omega_{\mathrm{sense}}|$, as in Fig. S6, but now for time resolved driving of the $|I_z\rangle \leftrightarrow |I_z-2\rangle$ transition. **(right)** The negative differential shift, $-\Delta\omega_{\mathrm{D}}$, as in Fig. S6, except we instead must calculate population in the $|I_z-2\rangle$ state, $\rho_{-2} = -\Delta\omega_{\mathrm{D}}/4A_{\mathrm{As}}$.

$$\begin{aligned} H_{\mathrm{tot}} =& \delta S_z + \Omega S_x + \omega_{\mathrm{n,As}} I_{z,\mathrm{As}} + \omega_{\mathrm{n,In}} I_{z,\mathrm{In}} \\ & - 2S_z(A_{\mathrm{As}} I_{z,\mathrm{As}} + A_{\mathrm{In}} I_{z,\mathrm{In}}) \\ & + S_z \sum_j \sum_k A_{\mathrm{nc},j,k} \left(M^+_{j,k} + M^-_{j,k} \right) \end{aligned} \tag{11}$$

The terms $\delta S_z + \Omega S_x$ are control of the electronic spin $S_i = \sigma_i/2$ (σ_i are the Pauli operators), which is split by ω_{e} by an external magnetic field B_z, and addressed in the spin's rotating frame via a resonant drive with Rabi frequency Ω and detuning δ (we have made the rotating-wave approximation); the drive comes from an optically stimulated Raman process[1,2]. The collective states of the nuclear spins are captured by the projection of their total angular momentum along the external field, i.e. their polarizations $I_{z,\mathrm{As}}$ and $I_{z,\mathrm{In}}$. The Zeeman effect on the nuclei is represented by $\omega_{\mathrm{n,As}} I_{z,\mathrm{As}} + \omega_{\mathrm{n,In}} I_{z,\mathrm{In}}$, where $\omega_{\mathrm{n,As}}$ and $\omega_{\mathrm{n,In}}$ are the nuclear Zeeman frequencies for As and In, respectively. The contact hyperfine interaction between the electron and the nuclei takes the form $-2S_z(A_{\mathrm{As}} I_{z,\mathrm{As}} + A_{\mathrm{In}} I_{z,\mathrm{In}})$, where A_{As} and A_{In} are the hyperfine constants per nuclear spin, and we have considered a homogeneous interaction between the electron and the nuclear spins. The quantity $\delta_{\mathrm{OH}} = -2(A_{\mathrm{As}} I_{z,\mathrm{As}} + A_{\mathrm{In}} I_{z,\mathrm{In}})$, called the Overhauser field, acts equivalently to a drive detuning and is notated as such. Here we have ignored the transverse part of the hyperfine interaction, which at high magnetic field is suppressed by $1/\omega_{\mathrm{e}}$. Equivalently, one can see that these transverse terms will rotate at the electronic Zeeman frequency when transformed to the electron's rotating frame, and thus average to zero[10]. The energy level diagram (in the lab frame) is shown in Fig. S8.

The noncollinear Hamiltonian $A_{\mathrm{nc},j,k} S_z M^{\pm}_{j,k}$ arises from dressing the hyperfine term $-2S_z A_j I_{z,j}$ with strain-induced quadrupolar nuclear effects[1,2,9,11,12]. The operators $M^{\pm}_{j,k}$ allow a change in the collective nuclear projection $I_{z,j}$ of species j – nuclear magnon (spin-wave) modes of two polarities ($\pm$) and two types of angular-momentum change (one unit $k=1$ or two units $k=2$) – when coupled with an electron spin flip in the driven (dressed-state) basis; in other words a Hartmann-Hahn resonance $\Omega^2 + \delta^2 = \omega^2_{\mathrm{n},j}$. The strength of this interaction is captured by the noncollinear hyperfine constant $A_{\mathrm{nc},j,k} = \sqrt{g(I_j)N_j}\,(A_j B_{\mathrm{Q},j}/\omega_{\mathrm{n},j})\,f(\theta_j)$, where we have used a $\sqrt{N_j}$ collective enhancement according to the number of nuclei of each species N_j[13]. $B_{\mathrm{Q},j}$ and $\pi/2-\theta_j$ are the quadrupolar interaction energy and quadrupolar angle relative to the external magnetic field. The scaling factor $g(I_j)$ is a function of the total spin of each species, $g(I_{\mathrm{As}}=3/2)=6$ and $g(I_{\mathrm{In}}=9/2)=1584/5$, and is derived from the quadrupolar nature of the magnon operators[2]. f is a trigonometric function of the quadrupolar angle θ_j. The Hamiltonian in Eq. 11 is the one used for numerical simulations.

Approximate Hamiltonian

In the main text, we have simplified the Hamiltonian by further dressing the driven electron with the noncollinear Hamiltonian[1,11], which is valid in proximity of the Hartmann-Hahn resonance, $\delta^2 + \Omega^2 \approx \omega^2_{\mathrm{n},j}$. This yields the electron-activated exchange term $-\sum_{j,k} \eta_{j,k} \Omega S_y M^{\pm}_{j,k}$, where the driven electron is more explicit (i.e. ΩS_y). The simplified Hamiltonian, per nuclear species j, then becomes:

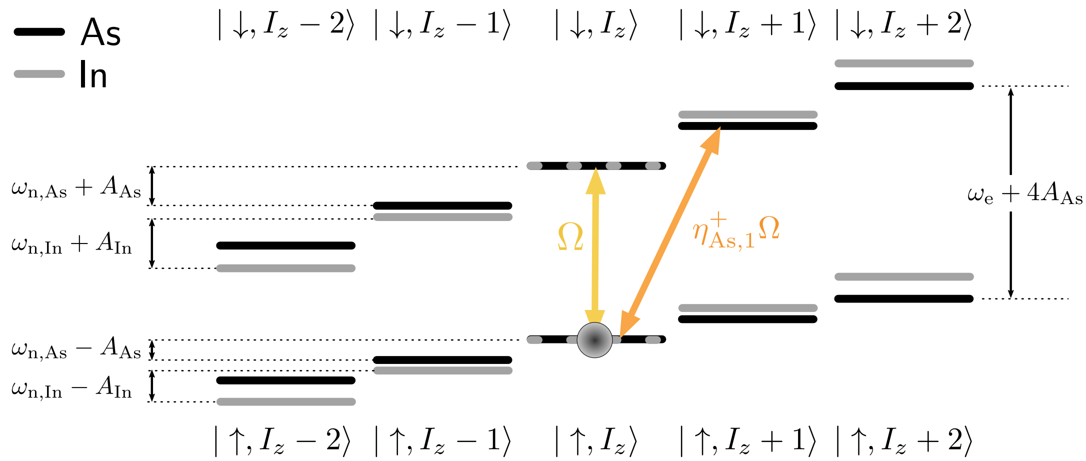

Fig.S8. **Magnon level scheme.** Lab-frame eigenstates of the undriven electron spin dressed with collective nuclear states, I_z, of arsenic (black) and indium (grey). Yellow arrow represents qubit drive with Rabi frequency Ω, which in turn activates the magnon injection (orange arrow) thanks to the quadrupolar-enabled noncollinear hyperfine interaction. The ladder of states is anharmonic since the dressed electronic excited (ground) state shifts by $\omega_{\mathrm{n},j}I_{z,j}+A_jI_{z,j}$ $(\omega_{\mathrm{n},j}I_{z,j}-A_jI_{z,j})$, for nuclear species j.

$$\begin{aligned}H =&\delta S_z+\Omega S_x+\omega_{\mathrm{n},j}I_{z,j}\\&-2S_zA_jI_{z,j}\\&-\sum_{k=1}^{2}\eta_{j,k}\Omega S_y M^{\pm}_{j,k}\end{aligned}$$

For clarity, the Hamiltonian of equation 1 in the main text considers only a single nuclear species, thus suppressing index j, and by assuming proximity to the resonance $\delta^2+\Omega^2\approx\omega_{\mathrm{n}}^2$, we take only the $k=1$ mode (and so suppress index k). In this parametrization, the strength of the electron activated exchange terms, relative to driving the ESR resonantly at Rabi frequency Ω, is conveniently captured by the dimensionless parameters $\eta^{\pm}_{j,k}$:

$$\begin{aligned}\eta^{\pm}_{\mathrm{As},1}=&\frac{A_{\mathrm{nc,As},1}}{\omega_{\mathrm{n,As}}}=\frac{A_{\mathrm{As}}B_{\mathrm{Q,As}}}{\omega^2_{\mathrm{n,As}}}\sqrt{6N_{\mathrm{As}}}\sin(2\theta_{\mathrm{As}})\\ \eta^{\pm}_{\mathrm{As},2}=&\frac{A_{\mathrm{nc,As},2}}{2\omega_{\mathrm{n,As}}}=\frac{A_{\mathrm{As}}B_{\mathrm{Q,As}}}{2\omega^2_{\mathrm{n,As}}}\sqrt{6N_{\mathrm{As}}}\cos^2(\theta_{\mathrm{As}})\\ \eta^{\pm}_{\mathrm{In},1}=&\frac{A_{\mathrm{nc,In},1}}{\omega_{\mathrm{n,In}}}=\frac{A_{\mathrm{In}}B_{\mathrm{Q,In}}}{\omega^2_{\mathrm{n,In}}}\sqrt{\frac{1584N_{\mathrm{In}}}{5}}\sin(2\theta_{\mathrm{In}})\\ \eta^{\pm}_{\mathrm{In},2}=&\frac{A_{\mathrm{nc,In},2}}{2\omega_{\mathrm{n,In}}}=\frac{A_{\mathrm{In}}B_{\mathrm{Q,In}}}{2\omega^2_{\mathrm{n,In}}}\sqrt{\frac{1584N_{\mathrm{In}}}{5}}\cos^2(\theta_{\mathrm{In}}).\end{aligned}$$

B. Master equation

We calculate the evolution of the system according to the following master equation:

$$\begin{aligned}\frac{\partial\rho(t|\delta_{\mathrm{OH}})}{\partial t}=&\,i[\rho(t|\delta_{\mathrm{OH}}),H_{\mathrm{tot}}(\delta_{\mathrm{OH}})]\\&+\sum_{j\in(\mathrm{As,In})}\sum_{l=-2}^{2}L(\sqrt{\frac{\Gamma_{\mathrm{n},j}}{2}}|I_{z,j}+l\rangle\langle I_{z,j}+l|)\\&+L(\sqrt{\frac{\Gamma_e}{2}}\sigma_z)\\&+L(\sqrt{\frac{\Omega}{2Q}}\sigma_x)\\&+L(\sqrt{\frac{\Gamma_{\mathrm{p}}}{2}}\sigma_+)\end{aligned}\tag{12}$$

where $\rho(t|\delta_{\mathrm{OH}})$ is the density operator conditional on an initial detuning caused by the Overhauser field $\delta_{\mathrm{OH}}=-2(A_{\mathrm{As}}I_{z,\mathrm{As}}+A_{\mathrm{In}}I_{z,\mathrm{In}})$; H_{tot} is given by Eq. 11; $L(a)=a\rho(t|\delta_{\mathrm{OH}})a^\dagger-\{a^\dagger a,\rho(t|\delta_{\mathrm{OH}})\}/2$ is the Lindblad operator; Γ_{n} is a broadening of the collective nuclear states, which acts as a pure dephasing term on the nuclei; Γ_e is a pure dephasing rate on the electron, $L(\sigma_z)$. Importantly, the sum effect of electron and nuclear dephasing terms are constrained in simulation to replicate the experimental measurement via a Hahn Echo of $T_2=2000\,\mathrm{ns}$, the electron's homogeneous dephasing time. Ω/Q represents a non-resonant, optical power-dependent electron spin relaxation mechanism, $L(\sigma_x)$, where $Q=Q(\Delta)$ is a proportionality factor between the relaxation rate and our optically-driven ESR that will depend on the Raman laser detuning Δ, as identified in our previous work[2]; and Γ_{p} is an optical electron spin pumping term, $L(\sigma_+)$, that is turned on when initialising the electron and cooling the nuclear ensemble.

C. Simulation

We use the QuTip[14] package for numerical integration of our quantum master equation. Each step of our pulse sequence is simulated using the master equation solver with the appropriately tuned Hamiltonian and dephasing terms, as per Eq. 12.

To make the calculation tractable, we truncate the Hilbert space of the problem to capture only first-order transitions $M^{\pm}_{j,k}$ ($k \in 1,2$): we calculate the dynamics for each species, j, only over the corresponding five-dimensional subspace $\{|I_{z,j}+l\rangle : l=-2,-1,0,+1,+2\}$, as shown in Fig. S8.

1. Initial State and electron T_2^*

The initial nuclear state is modelled in the following way. Following the nuclear preparation step, our system does not start out in a pure state of the nuclear ensemble from the perspective of its complete degrees of freedom in the single-spin picture. It does however start in a very well defined state of total nuclear polarisation I_z via the Overhauser shift locking that underlies our nuclear preparation, and results in nuclear-state narrowing. In fact, our nuclear preparation[1] narrows the distribution of nuclear polarisation I_z by approximately a factor 20 from its distribution at thermal equilibrium at 4 K. In our model, the only nuclear degree of freedom that we take into account is the nuclear polarisation I_z, treating it as a well defined quantum number for each species. Thus, within our model, the initial narrowed nuclear state is justifiably treated as resembling a pure state. This said, our nuclear preparation is not perfect, and leaves some slow fluctuations in I_z; meaning that within our model, I_z is partially mixed.

Our numerical treatment reflects this in the following way. A partially mixed state in the density matrix representation would sample the extrema of the Hilbert space and lead to edge-related aberrations. To avoid this we first take the initial nuclear density operator to be a pure state $|\uparrow, I_{z,\mathrm{As}}, I_{z,\mathrm{In}}\rangle$ (where the Overhauser shift $\delta_{\mathrm{OH}} = -2[A_{\mathrm{As}}I_{z,\mathrm{As}}+A_{\mathrm{In}}I_{z,\mathrm{In}}]$ equals zero). We then capture the effect of Overhauser field fluctuations – leading to inhomogeneous dephasing of the electron spin (T_2^*) – by averaging over many realizations of the above master equation for values of δ_{OH} taken uniformly from the cooled Overhauser distribution

$$p(\delta_{\mathrm{OH}}) = \frac{1}{\sqrt{2\pi\sigma_{\mathrm{OH}}^2}} e^{-\left(\frac{\delta_{\mathrm{OH}}}{\sqrt{2}\sigma_{\mathrm{OH}}}\right)^2},$$

where $\sigma_{\mathrm{OH}} = \frac{\sqrt{2}}{2\pi T_2^*}$. The ensemble density operator as a function of time, $\chi(t)$, is then calculated by averaging the conditional density operator $\rho(t|\delta_{\mathrm{OH}})$ over the different initial configurations:

$$\chi(t) = \int \mathrm{d}\delta_{\mathrm{OH}}\, p(\delta_{\mathrm{OH}})\rho(t|\delta_{\mathrm{OH}}).$$

2. Simulation results

Figures S9 and S10 present the full results for a simulation as a function of drive time, where the system variables are extracted directly following magnon injection and following a side-of-fringe Ramsey sequence, as executed experimentally in the context of Fig. 4 of the main text. In both figures, we show the electron polarisation (a), and the indium and arsenic polarisations separately (b) directly following magnon injection; and we show the electron polarisation after a reference and sense Ramsey (c), and the resulting differential shift (d). In Fig. S9, $\Omega = 34$ MHz and $\delta = -21$ MHz, which targets the Hartmann-Hahn resonance condition with the indium first sideband at $-\omega_{\mathrm{In}} = -42$ MHz, as reported via the differential shift in Fig. 4b of the main text. In Fig. S10, $\Omega = 35$ MHz and $\delta = -55$ MHz, which targets the Hartmann-Hahn resonance condition with the arsenic second sideband at $-2\omega_{\mathrm{As}} = -65$ MHz, as reported via the differential shift in Fig. 4c of the main text.

3. Coherence times

The electronic dephasing parameters that transpire from our simulation Eq. 12 are verified against two independently measured experimental quantities: the inhomogeneous dephasing time T_2^*, which we obtain by simulating a Ramsey experiment; the homogeneous dephasing time T_2, which we obtain by simulating a Hahn Echo. In both cases the simulation parameters are constrained such that these values agree with experimentally measured parameters.

4. Spectrum

We obtain our simulated spectrum (Fig. 2c main text) by implementing the following pulse sequence: *Reference* Ramsey sequence, electron re-initialization, magnon sideband drive at a fixed drive time and Rabi frequency Ω (same as experiment) and a variable detuning δ, electron re-initialization, *sense* Ramsey sequence. At each step, and in particular after the *sense* Ramsey sequence, we can extract the electron polarization $S = 2\langle S_z\rangle$ from the average density matrix $\chi(t)$, and plot it versus drive detuning δ.

5. Time dependence

We obtain our simulated drive-time dependence (Fig. 4b,c main text) by implementing the following pulse

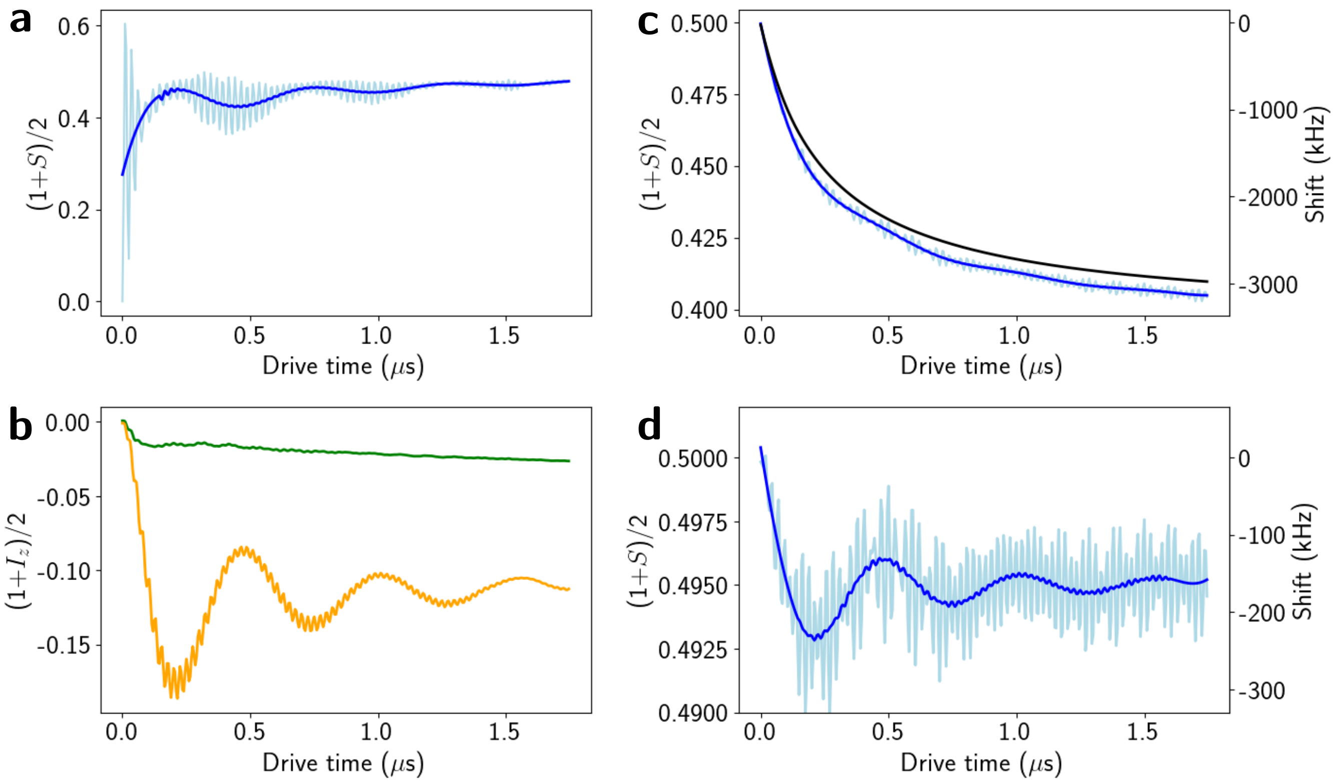

Fig.S9. **Simulation results. a,** electron polarization directly following magnon injection (light blue). The dark blue curve is the same passed through a third-order Savitzky-Golay filter with a 300 ns window. **b,** indium (orange) and arsenic (green) nuclear polarization directly following magnon injection **c,** electron polarization following side-of-fringe Ramsey, *reference* before magnon injection (black) and *sense* following magnon injection (light blue). The dark blue curve is the *sense* passed through a third-order Savitzky-Golay filter with a 300 ns window. **d,** difference between the *sense* and *reference* curves from **c**. The dark blue curve is the same passed through a third-order Savitzky-Golay filter with a 300 ns window. Simulation parameters for all curves: $\Omega = 34\,\mathrm{MHz}$, $\delta = -24\,\mathrm{MHz}$, $\omega_{\mathrm{n,In}} = 42\,\mathrm{MHz}$, $\omega_{\mathrm{n,As}} = 32.5\,\mathrm{MHz}$, $N_{\mathrm{In}} = 364$, $N_{\mathrm{As}} = 342$, $A_{\mathrm{In}} = 0.4\,\mathrm{MHz}$, $A_{\mathrm{As}} = 1.35\,\mathrm{MHz}$, $B_{Q,\mathrm{In}} = 1\,\mathrm{MHz}$, $B_{Q,\mathrm{As}} = 1\,\mathrm{MHz}$, $\theta_{\mathrm{In}} = 25^\circ$, $\theta_{\mathrm{As}} = 25^\circ$, $T_2^* = 32\,\mathrm{ns}$, $T_2 = 2000\,\mathrm{ns}$, $Q = 45$, $\Gamma_{\mathrm{n,As}} = 0.05\,\mathrm{MHz}$, $\Gamma_{\mathrm{n,In}} = 0.06\,\mathrm{MHz}$.

sequence: *Reference* Ramsey sequence, electron re-initialization, magnon sideband drive at a fixed detuning δ and Rabi frequency Ω (matching the experimental settings) and for a variable drive time T, electron re-initialization, *sense* Ramsey sequence. At each step, and in particular after the *sense* Ramsey sequence, we can extract the electron polarization $S = 2\langle S_z\rangle$ from the average density matrix $\chi(t)$, and plot it versus drive time T.

6. Effects of dynamic nuclear polarization

In our simulations we account for the effects of the MHz-scale dynamic nuclear polarization present during our experiments (as reported in Fig. 3 of the main text) by fitting our experimental *reference* signal as a function of drive time T. We then feed this into our simulation as a drive-time dependent detuning $\delta(T)$. As an example, this is shown in Figs. S9c and S10c, where the simulated *reference* signal (black curve) depends on drive time and reproduces the expected MHz-scale ESR shift.

7. Effects of dephasing parameters

In Fig. S11, we explore the dependence of our simulated magnon dynamics – as seen via the differential Ramsey signal as in Fig. 4b,c of the main text – on four dephasing parameters: Γ_{n}, Γ_e, Q, and T_2^*. Our starting point is the set of parameters that results in the best fit to the data of Fig. 4b of the main text.

D. Summary of model parameters

1. Fixed parameters

In Table S1, we list the parameters which are used as fixed inputs to the model, based on previous studies or inferred from independent measurements.

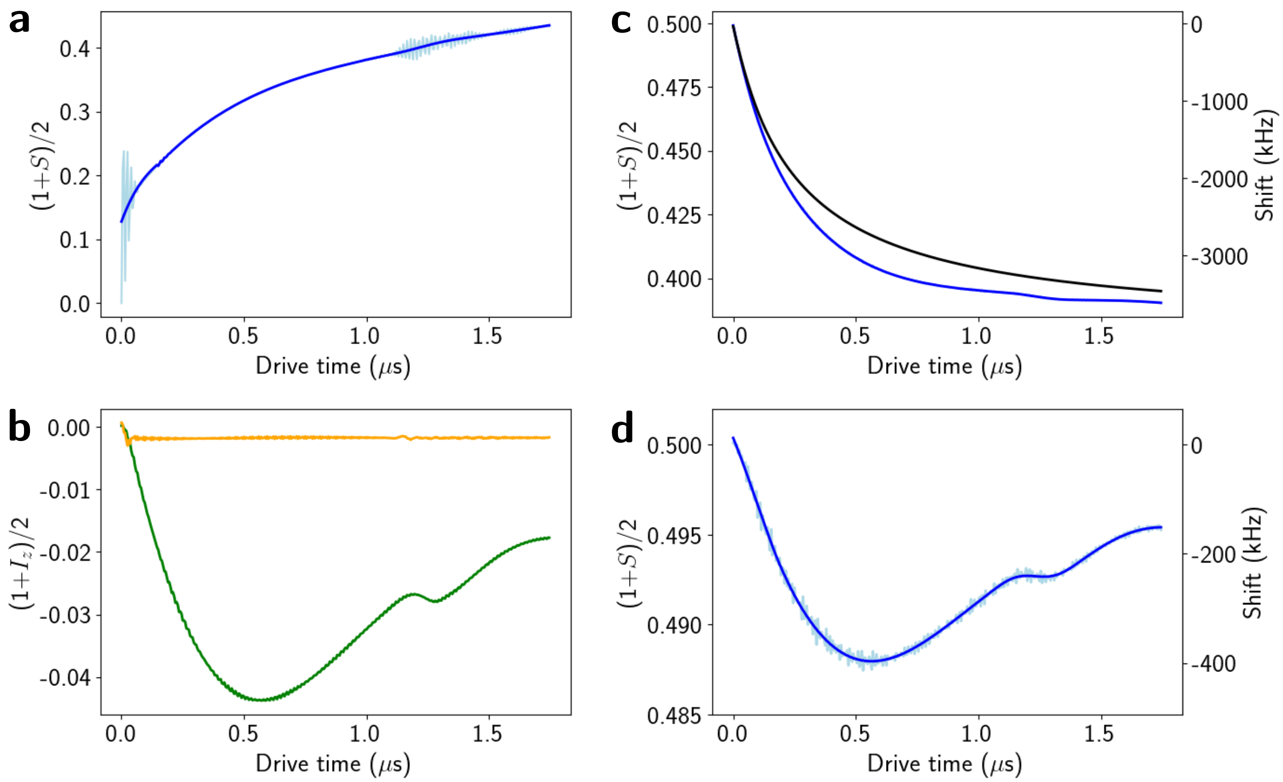

Fig.S10. **Simulation results. a,** electron polarization directly following magnon injection (light blue). The dark blue curve is the same passed through a third-order Savitzky-Golay filter with a 300 ns window. **b,** indium (orange) and arsenic (green) nuclear polarization directly following magnon injection **c,** electron polarization following side-of-fringe Ramsey, *reference* before magnon injection (black) and *sense* following magnon injection (light blue). The dark blue curve is the *sense* passed through a third-order Savitzky-Golay filter with a 300 ns window. **d,** difference between the *sense* and *reference* curves from **c**. The dark blue curve is the same passed through a third-order Savitzky-Golay filter with a 300 ns window. Simulation parameters for all curves: $\Omega = 35\,\mathrm{MHz}$, $\delta = -55\,\mathrm{MHz}$, $\omega_{\mathrm{n,In}} = 42\,\mathrm{MHz}$, $\omega_{\mathrm{n,As}} = 32.5\,\mathrm{MHz}$, $N_{\mathrm{In}} = 364$, $N_{\mathrm{As}} = 342$, $A_{\mathrm{In}} = 0.4\,\mathrm{MHz}$, $A_{\mathrm{As}} = 1.35\,\mathrm{MHz}$, $B_{Q,\mathrm{In}} = 1\,\mathrm{MHz}$, $B_{Q,\mathrm{As}} = 1\,\mathrm{MHz}$, $\theta_{\mathrm{In}} = 25°$, $\theta_{\mathrm{As}} = 25°$, $T_2^* = 32\,\mathrm{ns}$, $T_2 = 2000\,\mathrm{ns}$, $Q = 45$, $\Gamma_{\mathrm{n,As}} = 0.05\,\mathrm{MHz}$, $\Gamma_{\mathrm{n,In}} = 0.06\,\mathrm{MHz}$.

We discuss these fixed parameters here. From previous measurements of QDs on this wafer[15], we consider a QD composition of $\mathrm{In_{0.5}Ga_{0.5}As}$. Total hyperfine interaction strengths for InGaAs are well-known and size-independent constants: 11.1 GHz for arsenic and 13.5 GHz for indium[12]. Having pinned the composition, we can then calculate the number of nuclei in the QD from a measurement of the electron spin decoherence time $T_{2,\mathrm{pre}}^* = 1.7\,\mathrm{ns}$ (from previous work[1] on the same QD); in this case it is measured without any prior preparation of the nuclear spins to assess the "natural" width of the Overhauser field distribution[12,15]. Using a Gaussian electronic wavefunction whose standard deviation is half of the QD radius, we find that the dot must contain approximately 80,000 nuclei. Accordingly, the number of arsenic nuclei is $N_{\mathrm{As}}^{\mathrm{tot}} = 40{,}000$ and the number of indium nuclei is $N_{\mathrm{In}}^{\mathrm{tot}} = 20{,}000$. Also present are 20,000 gallium nuclei, which we ignore in the magnon dynamics due to their typically much weaker quadrupolar contributions[15]. To be precise, taking typical values for the quadrupolar interaction energies, $B_{Q,j}$, and quadrupolar angles, θ_j,[7] we calculate the transition strength for gallium relative to that of arsenic: approximately 15 times weaker for $I_z \to I_z \pm 1$, and 4 times weaker for $I_z \to I_z \pm 2$. Given arsenic's already weak transition strength on the $I_z \pm 2$ transition relative to the dephasing rates in the system (main text Fig. 4c), we can safely neglect all magnon modes of gallium. We fix the quadrupolar energy to be $B_{\mathrm{Q}} = 1\,\mathrm{MHz}$ for both indium and arsenic, as consistent with previous measurements[1,2,11,15]; to fit our data, the strength of the noncollinear interactions is varied instead via the collective enhancement, which is of order $\sqrt{N}$. We use nuclear gyromagnetic ratios of 7.22 MHz/T for arsenic, and 9.33 MHz/T for indium, to obtain our Zeeman energy splittings at 4.5 T of $\omega_{\mathrm{n,As}} = 32.5\,\mathrm{MHz}$ and $\omega_{\mathrm{n,In}} = 42\,\mathrm{MHz}$. The Hahn echo $T_2 = 2000 \pm 100\,\mathrm{ns}$ of the electron spin was also measured in previous work[1]. The Q factor of Rabi oscillations, equivalent to optically induced electron spin relaxation (T_1) is measured directly from the spectrum data of Fig. 2c in the main text; for

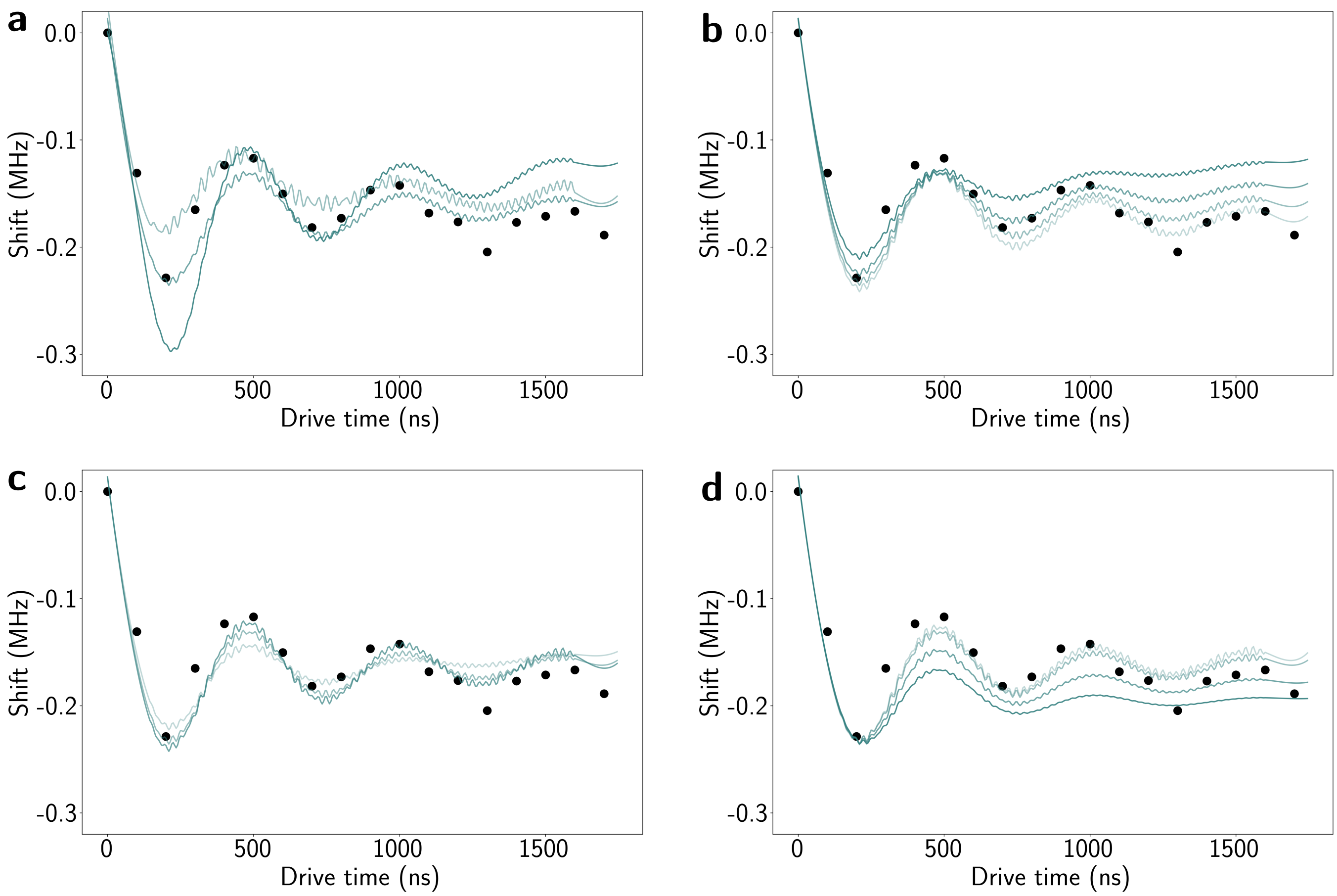

Fig.S11. **Effects of dephasing in simulations.** Black data points in all data are those reported in Fig. 4b of the main text ($\Omega = 34\,\mathrm{MHz}$, $\delta = 21\,\mathrm{MHz}$). Simulation parameters for all curves, unless otherwise stated: $\Omega = 34\,\mathrm{MHz}$, $\delta = 24\,\mathrm{MHz}$, $\omega_{\mathrm{n,In}} = 42\,\mathrm{MHz}$, $\omega_{\mathrm{n,As}} = 32.5\,\mathrm{MHz}$, $N_{\mathrm{In}} = 364$, $N_{\mathrm{As}} = 342$, $A_{\mathrm{In}} = 0.4\,\mathrm{MHz}$, $A_{\mathrm{As}} = 1.35\,\mathrm{MHz}$, $B_{Q,\mathrm{In}} = 1\,\mathrm{MHz}$, $B_{Q,\mathrm{As}} = 1\,\mathrm{MHz}$, $\theta_{\mathrm{In}} = 25°$, $\theta_{\mathrm{As}} = 25°$, $T_2^* = 32\,\mathrm{ns}$, $T_2 = 2000\,\mathrm{ns}$, $Q = 45$, $\Gamma_{\mathrm{n,As}} = 0.05\,\mathrm{MHz}$, $\Gamma_{\mathrm{n,In}} = 0.06\,\mathrm{MHz}$. All simulations are passed through a third-order Savitzky-Golay filter with a 300 ns window. **a,** from light to dark: $T_2^* = 15\,\mathrm{ns}$, $T_2^* = 30\,\mathrm{ns}$, $T_2^* = 60\,\mathrm{ns}$. **b,** from light to dark: $\Gamma_e = 0.1\,\mu\mathrm{s}^{-1}$, $\Gamma_e = 0.45\,\mu\mathrm{s}^{-1}$, $\Gamma_e = 1\,\mu\mathrm{s}^{-1}$, $\Gamma_e = 2\,\mu\mathrm{s}^{-1}$. **c,** from light to dark: $Q = 20$, $Q = 45$, $Q = 100$. **d,** from light to dark: $\Gamma_{\mathrm{n}} = 0.001\,\mathrm{MHz}$, $\Gamma_{\mathrm{n}} = 0.05\,\mathrm{MHz}$, $\Gamma_{\mathrm{n}} = 0.25\,\mathrm{MHz}$, $\Gamma_{\mathrm{n}} = 0.5\,\mathrm{MHz}$.

these data, the far-detuned electron spin polarization, $S \approx -0.6$ after 1800 ns of drive time at $\Omega = 8\,\mathrm{MHz}$, sets a relaxation rate of $\Omega/Q = \Omega/45 \approx 180\,\mathrm{kHz}$. The Rabi frequency of $\Omega_{\mathrm{cool}} = 13\,\mathrm{MHz}$ and optical pumping rate of $\Gamma_{\mathrm{p}} = 35\,\mathrm{MHz}$ during nuclear spin cooling are known from Rabi oscillation and optical saturation calibration measurements, respectively. Following this preparation we measure electron spin decoherence time $T_2^* \approx 30\,\mathrm{ns}$ in a Ramsey measurement, as presented in Fig. 1 of the main text.

2. *Fitted parameters*

In Tables S2 and S3, we list the parameters which are used as free parameters in the model. Table S2 reports the parameter values used in fitting the magnon spectrum of Fig. 2 in the main text. Table S3 reports the parameter values used in fitting the magnon dynamics of Fig. 4 in the main text.

The single-nucleus hyperfine constants we report in the main text, A_{As} and A_{In}, are from the fits to the spectra of Fig. 2c (electron polarization) and Fig. 2e (differential shift); we also report these values in Table S2. A_{As} and A_{In} can also be fitted independently from the Rabi oscillations of Fig. 4b (indium $I_z \to I_z - 1$ transition) and Fig. 4c (arsenic $I_z \to I_z - 2$ transition); we report these values in Table S3 with errors representing one standard deviation of uncertainty on the mean. As a result, the values of A_{As} and A_{In} obtained from the spectrum (Fig. 2) are found to agree statistically with values obtained from Rabi oscillations (Fig. 4) within two standard deviations for arsenic and one standard deviation for indium. It is noteworthy that as direct observations of the hyperfine shift, the observed Ramsey shifts of Fig. 2e, Fig. 4b, and Fig. 4c strongly constrain the fitted values of A_{As} and A_{In} in our model.

The quadrupolar angles θ_{As} and θ_{In} are most strongly constrained in the fit to the spectrum of Fig. 2c (electron polarization), since within a species the ratio of non-collinear hyperfine constant for $I_z \pm 1$ to $I_z \pm 2$ processes is fixed to $2\sin(2\theta)/\cos^2(\theta)$. We find an angle of 25° for both species, which sets this ratio to 1.87 as evidenced in the magnon sidebands of Fig. 2c. We keep these values fixed when fitting the magnon dynamics of Fig. 4.

The magnon participation ratios $N_{\mathrm{As}}/N_{\mathrm{As}}^{\mathrm{tot}}$ and $N_{\mathrm{In}}/N_{\mathrm{In}}^{\mathrm{tot}}$ represent the fraction of nuclei partaking in the arsenic and indium magnon modes, respectively, and are defined as the fitted number of nuclei over the number of nuclei estimated from a measurement of T_2^* (see Table S1). This parameter, tuned individually for each species, is how the activated exchange frequency can be fitted. Making this parameter a function of drive Ω captures the drive-dependence of the activated exchange frequency, as described in the context of Fig. 4d of the main text and of section VIII of this document.

Finally, we note that the nuclear dephasing rate, Γ_{n}, reported in table S3, which dictates the magnon coherence time, is only one of the rates contributing to the damping of the electron-nuclear dynamics (see Eq. 12). In fact, the independently measured electronic relaxation, parametrised by Q, and dephasing rates, parametrised by T_2 and T_2^*, are already sufficient to capture the damping of the *activated exchange*. As such, we can only conclude with confidence a lower bound for the magnon coherence time, which must be longer than that of the electron.

TABLE S1. Summary of independently measured or fixed model parameters

Indium concentration $\mathrm{In}_x\mathrm{Ga}_{1-x}\mathrm{As}$, x	0.5
Zeeman energy (at 4.5 T), $\omega_{\mathrm{n,As}}$, arsenic	32.5 MHz
Zeeman energy (at 4.5 T), $\omega_{\mathrm{n,In}}$, indium	42 MHz
Total hyperfine interaction, arsenic	11.1 GHz
Total hyperfine interaction, indium	13.5 GHz
Quadrupolar constant, arsenic, $B_{\mathrm{Q,As}}$	1 MHz
Quadrupolar constant, indium, $B_{\mathrm{Q,In}}$	1 MHz
Electronic decoherence time, pre-cooling, $T_{2,\mathrm{pre}}^*$	1.7 ns
Electronic decoherence time, post-cooling, T_2^*	32 ns
Electronic Hahn Echo time, T_2	2000 ns
Electronic Rabi Quality Factor, Q	45
Optical pumping rate (cooling), Γ_{p}	35 MHz
Cooling Rabi frequency, Ω_{cool}	13 MHz
Total number of nuclei, $N_{\mathrm{As}}^{\mathrm{tot}}$, arsenic	40,000
Total number of nuclei, $N_{\mathrm{In}}^{\mathrm{tot}}$, indium	20,000

TABLE S2. Summary of fitted model parameters, magnon spectrum, main text Fig. 2

Magnon participation ratio, arsenic, $N_{\mathrm{As}}/N_{\mathrm{As}}^{\mathrm{tot}}$	0.05
Magnon participation ratio, indium, $N_{\mathrm{In}}/N_{\mathrm{In}}^{\mathrm{tot}}$	0.029
Hyperfine constant per arsenic nucleus, A_{As}	950 kHz
Hyperfine constant per indium nucleus, A_{In}	550 kHz
Quadrupolar angle, arsenic, θ_{As}	25°
Quadrupolar angle, indium, θ_{In}	25°
Nuclear dephasing, arsenic, $\Gamma_{\mathrm{n,As}}$	0.5 MHz
Nuclear dephasing, indium, $\Gamma_{\mathrm{n,In}}$	0.6 MHz

TABLE S3. Summary of fitted model parameters, magnon dynamics, main text Fig. 4

Magnon participation ratio, arsenic, $N_{\mathrm{As}}/N_{\mathrm{As}}^{\mathrm{tot}}$	0.0045
Magnon participation ratio, indium, $N_{\mathrm{In}}/N_{\mathrm{In}}^{\mathrm{tot}}$	0.006-0.018
Hyperfine constant per arsenic nucleus, A_{As}	1350(200) kHz
Hyperfine constant per indium nucleus, A_{In}	500(60) kHz
Nuclear dephasing, arsenic, $\Gamma_{\mathrm{n,As}}$	0.05 MHz
Nuclear dephasing, indium, $\Gamma_{\mathrm{n,In}}$	0.06 MHz

E. Estimate of bipartite electron-nuclear entanglement

Having measured coherent oscillations between the initial state, $|\uparrow, I_{z,\mathrm{In}}\rangle$, and a target state, $|\downarrow, I_{z,\mathrm{In}}-1\rangle$, in Fig. 4b of the main text, the finite visibility we observe

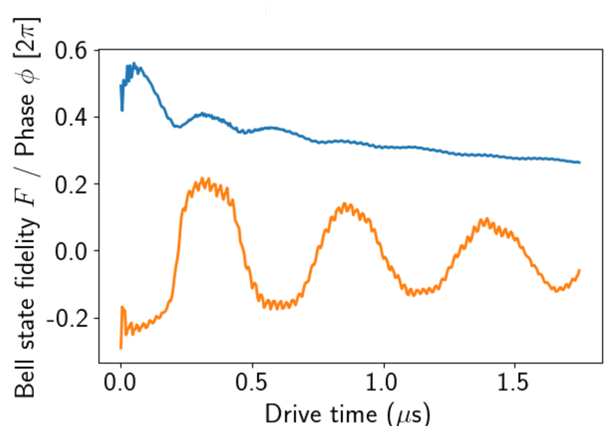

Fig.S12. Bell state fidelity and phase. Fidelity $\mathcal{F}$ (blue) and Bell state $|\psi_\phi\rangle$ phase ϕ (orange) as a function of drive time. Simulation parameters: $\Omega = 34$ MHz, $\delta = 24$ MHz, $\omega_{\mathrm{n,In}} = 42$ MHz, $\omega_{\mathrm{n,As}} = 32.5$ MHz, $N_{\mathrm{In}} = 364$, $N_{\mathrm{As}} = 342$, $A_{\mathrm{In}} = 0.4$ MHz, $A_{\mathrm{As}} = 1.35$ MHz, $B_{Q,\mathrm{In}} = 1$ MHz, $B_{Q,\mathrm{As}} = 1$ MHz, $\theta_{\mathrm{In}} = 25°$, $\theta_{\mathrm{As}} = 25°$, $T_2^* = 32$ ns, $T_2 = 2000$ ns, $Q = 45$, $\Gamma_{\mathrm{n,As}} = 0.05$ MHz, $\Gamma_{\mathrm{n,In}} = 0.06$ MHz.

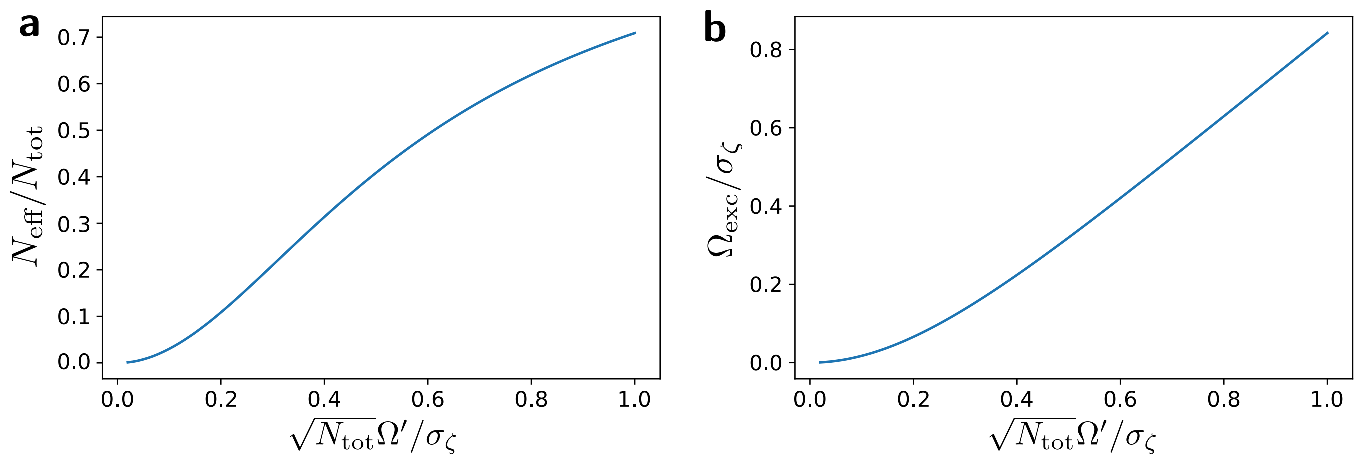

Fig.S13. **Collective Rabi oscillations with inhomogeneities. a,** Effective number of nuclei in the magnon mode as a function of the normalized maximal collective Rabi frequency $\sqrt{N_{\rm tot}}\Omega'/\sigma_\zeta$. **a,** Normalized electron-nuclear exchange frequency, $\Omega_{\rm exc}/\sigma_\zeta$, as a function of the normalized maximal collective Rabi frequency $\sqrt{N_{\rm tot}}\Omega'/\sigma_\zeta$.

is a witness of bipartite entanglement between the electron and the magnon mode. This finite visibility is in fact a model-independent signature that quantum correlations must exist. Having fitted our experimental data with the observables extracted from the average density matrix $\chi(t)$, it is also possible to quantify this visibility using our simulated density matrix. To do so, we define a target Bell state of form,

$$|\psi_\phi\rangle = |\tilde{\uparrow}, I_{z,\rm In}\rangle + e^{i\phi}\,|\tilde{\downarrow}, I_{z,\rm In}-1\rangle\,,$$

which is nothing more than a choice of basis for the bipartite electron-magnon system. Here we have expressed the electron state in the dressed state basis,

$$\begin{aligned}|\tilde{\uparrow}\rangle &= \cos(\theta/2)\,|{\uparrow}\rangle + \sin(\theta/2)\,|{\downarrow}\rangle\\ |\tilde{\downarrow}\rangle &= \cos(\theta/2)\,|{\downarrow}\rangle - \sin(\theta/2)\,|{\uparrow}\rangle\,,\end{aligned}$$

where $\sin(\theta) = \Omega/\sqrt{\Omega^2+\delta^2}$. We then get our metric of visibility from the overlap fidelity,

$$\mathcal{F} = \max_\phi \langle\psi_\phi|\,\chi(t)\,|\psi_\phi\rangle\,.$$

In Fig. S12, we show the dependence of the fidelity $\mathcal{F}$ and state phase ϕ on drive time for the experiment performed in the context of Fig. 4b of the main text, whose full simulation results are shown in Fig. S9. The values shown in the inset of Fig. 4d of the main text are the maxima of fidelity across drive time.

VIII. COLLECTIVE RABI OSCILLATIONS WITH INHOMOGENEOUS BROADENING

In the experiments, we measure a collective mode characterized by an electron-nuclear *activated exchange* frequency scaling as $\sqrt{N}\Omega'$, where Ω' is the single nucleus Rabi frequency (tuned by the ESR drive strength Ω). In the absence of inhomogeneities, all nuclei $N = N_{\rm tot}$ take part identically, leading to a simple linear dependence of the *activated exchange* frequency on the ESR drive strength Ω. However, in the presence of inhomogeneities, each nuclear spin couples to the ESR drive field differently due to its spectral detuning, ζ, as discussed already in Section V. However, the frequency scaling of the *activated exchange* in the presence of inhomogeneities still stays linear, albeit with a reduced number of nuclei, $N_{\rm eff} < N_{\rm tot}$. The superlinear scaling (with exponent value of 2.0 for the I_z-1 mode and 1.1 for the I_z-2 mode) observed in the experiments (Fig. 4d main text) is not captured by the basic assumption of noninteracting nuclei. This points towards an $N_{\rm eff}$ value that is actually not constant, but is increasing with the ESR drive strength. In other words, Fig. 4d of the main text suggests that more nuclei take part coherently in the collective magnon mode as the ESR drive strength is increased.

To mimic this behaviour, we introduce a transfer function whose width increases with the drive strength, Ω. By assuming for the magnon mode a Lorentzian spectrum of width $\sqrt{N_{\rm eff}}\Omega'$, we can calculate the number of nuclear spins comprising the magnon mode self-consistently via

$$N_{\rm eff} = N_{\rm tot}\int_{-\infty}^{\infty}\frac{N_{\rm eff}\Omega'^2}{N_{\rm eff}\Omega'^2+\zeta^2}S(\zeta)d\zeta\,, \qquad (13)$$

where $S(\zeta)$ is the detuning probability distribution characterising the nuclear inhomogeneities. When we assume this distribution to be a Gaussian function, $S(\zeta) = \frac{1}{\sqrt{\pi}\sigma_\zeta}\exp(-\zeta^2/\sigma_\zeta^2)$, the self-consistent $N_{\rm eff}$ above is equivalent to

$$\frac{N_{\rm eff}}{N_{\rm tot}} = \frac{\sqrt{\pi N_{\rm eff}}\Omega'}{\sigma_\zeta}\exp(\frac{N_{\rm eff}\Omega'^2}{\sigma_\zeta^2})\mathrm{erfc}(\frac{\sqrt{N_{\rm eff}}\Omega'}{\sigma_\zeta}) \qquad (14)$$

where erfc is the complementary error function. Solving this equation numerically, we find that the number of effective nuclei partaking in the collective mode N_{eff} increases with Ω', resulting in a superlinear increase of the collective Rabi frequency with the ESR drive strength (Fig. S13), qualitatively reproducing Fig. 4d of the main text.

We emphasize that this behaviour of N_{eff} is qualitatively robust and does not depend critically on the specific choice of transfer function, as long as its width increases with drive strength, nor on the detuning probability distribution $S(\zeta)$, chosen to be Gaussian here as an example. Such drive-dependent scaling of N_{eff} is a typical indication of synchronization (or entrainment) phenomena[16], which would indicate the presence of interactions among the nuclei. While the model in Section V of the SI does not include such interacting nuclei, a possible candidate to consider is the recently identified electron-mediated nuclear-nuclear interactions which scale as $A_j^2/\omega_{\mathrm{e}}$[17], analogous to the well-known RKKY interaction[18]. Identifying the exact mechanism of nonlinearity in Fig. 4 of the main text will require further theoretical and experimental investigations, but the sensing capability demonstrated in this work promises more insights into this matter in a near future.

1. Gangloff, D. A. *et al.* Quantum interface of an electron and a nuclear ensemble. *Science* **364**, 62–66 (2019).
2. Bodey, J. H. *et al.* Optical spin locking of a solid-state qubit. *npj Quantum Inf.* **5**, 95 (2019).
3. Degen, C. L., Reinhard, F. & Cappellaro, P. Quantum sensing. *Rev. Mod. Phys.* **89**, 035002 (2017).
4. Allan, D. W. Statistics of atomic frequency standards. *Proc. IEEE* **54**, 221–230 (1966).
5. Howe, D., Allan, D. & Barnes, J. Properties of signal sources and measurement methods. In *Thirty Fifth Annual Frequency Control Symposium*, 669–716 (IEEE, 2008).
6. Chekhovich, E. A. *et al.* Structural analysis of strained quantum dots using nuclear magnetic resonance. *Nat. Nanotechnol.* **7**, 646–650 (2012).
7. Bulutay, C. Quadrupolar spectra of nuclear spins in strained $\mathrm{In_xGa_{1-x}As}$ quantum dots. *Phys. Rev. B* **85**, 115313 (2012).
8. Bulutay, C., Chekhovich, E. A. & Tartakovskii, A. I. Nuclear magnetic resonance inverse spectra of InGaAs quantum dots: Atomistic level structural information. *Phys. Rev. B* **90**, 205425 (2014).
9. Denning, E. V., Gangloff, D. A., Atatüre, M., Mørk, J. & Le Gall, C. Collective quantum memory activated by a driven central spin. *Phys. Rev. Lett.* **123**, 140502 (2019).
10. Henstra, A. & Wenckebach, W. The theory of nuclear orientation via electron spin locking (NOVEL). *Mol. Phys.* **106**, 859–871 (2008).
11. Högele, A. *et al.* Dynamic nuclear spin polarization in the resonant laser excitation of an InGaAs quantum dot. *Phys. Rev. Lett.* **108**, 197403 (2012).
12. Urbaszek, B. *et al.* Nuclear spin physics in quantum dots: An optical investigation. *Rev. Mod. Phys.* **85**, 79–133 (2013).
13. Yang, W. & Sham, L. J. General theory of feedback control of a nuclear spin ensemble in quantum dots. *Phys. Rev. B* **88**, 235304 (2013).
14. Johansson, J., Nation, P. & Nori, F. QuTiP 2: A Python framework for the dynamics of open quantum systems. *Comput. Phys. Commun.* **184**, 1234–1240 (2013).
15. Stockill, R. *et al.* Quantum dot spin coherence governed by a strained nuclear environment. *Nat. Commun.* **7**, 12745 (2016).
16. Kuramoto, Y. Self-entrainment of a population of coupled non-linear oscillators. In *International Symposium on Mathematical Problems in Theoretical Physics*, 420–422 (Springer-Verlag, 2005).
17. Wüst, G. *et al.* Role of the electron spin in determining the coherence of the nuclear spins in a quantum dot. *Nat. Nanotechnol.* **11**, 885–889 (2016).
18. Ruderman, M. A. & Kittel, C. Indirect exchange coupling of nuclear magnetic moments by conduction electrons. *Phys. Rev.* **96**, 99–102 (1954).